Spatiotemporal computed tomography of dynamic processes

Anders Kaestner
Paul Scherrer Institute
Neutron Spallation Source Division
Villigen, CH5232, Switzerland
E-mail: anders.kaestner@psi.ch

Beat Münch
Pavel Trtik
Swiss Federal Laboratories for Materials Science and Technology Empa
Dübendorf, Switzerland

Les Butler
Louisiana State University
Chemistry Department
Baton Rouge, Louisiana

Abstract. Modern computed tomography (CT) equipment allowing fast 3-D imaging also makes it possible to monitor dynamic processes by 4-D imaging. Because the acquisition time of various 3-D–CT systems is still in the range of at least milliseconds or even hours, depending on the detector system and the source, the balance of the desired temporal and spatial resolution must be adjusted. Furthermore, motion artifacts will occur, especially at high spatial resolution and longer measuring times. We propose two approaches based on nonsequential projection angle sequences allowing a convenient postacquisition balance of temporal and spatial resolution. Both strategies are compatible with existing instruments, needing only a simple reprograming of the angle list used for projection acquisition and care with the projection order list. Both approaches will reduce the impact of artifacts due to motion. The strategies are applied and validated with cold neutron imaging of water desorption from originally saturated particles during natural air-drying experiments and with x-ray tomography of a polymer blend heated during imaging. [DOI: 10.1117/1.3660298]

Subject terms: computed tomography; motion artifacts; neutron imaging; x-ray imaging; dynamic processes; Greek golden ratio; binary decomposition.

Paper 110752RR received Jul. 1, 2011; revised manuscript received Oct. 17, 2011; accepted for publication Oct. 21, 2011; published online Dec. 5, 2011.

1 Introduction

Tomography of dynamic processes is a challenging task. In the best case, the acquisition system is so fast that the motion of the process is less than the spatial resolution of the imaging device. Then it is possible to acquire 3-D data without significant motion-related artifacts. This paper will focus on the case when the sample shape or material distribution changes significantly during the course of acquisition. Under such circumstances, motion artifacts will appear near the moving parts of the sample unless the acquisition protocol is modified to cope with the motion. In medical imaging where the motion is cyclic, the acquisition can be guided by a gating signal given by, e.g., the patients respiration.[1,2] This makes is possible to complete the projection data over several cycles of the process. The noncyclic case is intrinsically more difficult because the process is unlikely to return to the same condition again. Hence, each projection will contain new information about the progress of the studied process.

In this paper, two alternative strategies for the acquisition of projections for noncyclic processes are proposed (see Sec. 2). These strategies are based on nonsequential decompositions of the sample rotation angle sequence. In addition to making the reconstructions less sensitive to motion artifacts, these acquisition strategies also allow the reconstruction of subsets of the projection data with variable temporal resolution.

The performance of the schemes with respect to the occurrence of the motion artifacts in the reconstructed computed tomography (CT) images is compared to the standard sequential acquisition strategy on a series of air-drying experiments (see Sec. 3). An example with a polymer blend imaged during sample heating using synchrotron x-rays is also given. In Sec 4, the potential of the alternative strategies regarding the possibility of postacquisition selection of the appropriate spatial and temporal resolutions of the 3-D imaging of the dynamic process is investigated. Finally, the advantages and the drawbacks of the alternative acquisition strategies are discussed in Sec. 5.

0091-3286/2011/$25.00 © 2011 SPIE

2 Alternative Scan Decomposition Strategies

In computed tomography, a large number of projection images are captured from many different angular positions. Usually, these projections are distributed as a monotonic increasing (or decreasing) sequence over either the interval $[0,\pi)$ or $[0,2\pi)$, and with a constant angular increment between each projection.

The basic idea of the proposed alternative acquisition schemes is to adapt the angle sequence of projections so that subsets of chronologically contiguous projections contain sufficient information for reconstruction. These subsets can be interpreted as time frames. Thereby, it will be possible to select between high temporal resolution by reconstructing small time frames and high spatial resolution by reconstructing large time frames. The potential of such projection sets is illustrated in Fig. 1 by a pyramid with the ordinate symbolizing the temporal and the abscissa the spatial resolution. The top rectangle represents the reconstruction of the full data set resulting in the highest spatial resolution yet averaged over the entire time frame; the bottom rectangles feature the lowest spatial resolution but the highest time resolution.

By increasing the temporal resolution, the number of projections for each reconstruction decreases. This has the consequence that the projection data must be downsampled for the reconstruction to fulfill the requirement of the Nyquist theorem for tomography.[3] The following sections present two different methods to achieve the above benefits.

2.1 *Binary Decomposition*

The full binary decomposition scheme with K nesting levels consists of a set

$$S_1^K = \left\{s_1^0, s_2^0, \ldots, s_M^0\right\} \tag{1}$$

of M sequential sparse subscans $s_i^0 = \{\,\}$ with equidistant angles distributed over π, each

$$\Psi_i^0 = \{\beta_i + j \cdot \psi_\Delta \mid j \in [0, \ldots, N-1],\ i \in \mathbb{Z}^+\}, \tag{2}$$

where $\beta_i = i\psi_\Delta/M$ is the starting angle, $\psi_\Delta = \pi/N$ is the angular increment between two chronologically consequent projections, and N is the number of projections in the set s_i^0. Therefore, β_i are chosen such that binary counts 2^k of interleaved s_i^0 may be merged to new sets

$$S_i^k = \left\{s_i^0, \ldots, s_{i-1+2^k}^0\right\} \tag{3}$$

holding complete sets of $N2^k$ equispaced projection angles $\Psi_i^k \in [0, \pi)$, each. The nesting level $k \in [0, \ldots, K]$ implies the currently selected balance between spatial and temporal resolution: $S_i^{k=0}$ (i.e., the sparse subscans) contain the smallest spatial and the highest available temporal resolution, while $S_1^{k=K}$ at the topmost nesting level $K = \log_2(M)$ holds the highest spatial resolution with $N \cdot M$ projections, yet at only one single instant of time.

The sequence S_1^K is generated by starting with the set $\mathbf{A}_1 = \{0\}$ at $i = 1$ and iteratively expanding by

$$\mathbf{A}_{i+1} = \left\{\mathbf{A}_i,\ \ \mathbf{A}_i + \frac{M}{2^i}\right\}. \tag{4}$$

The angular sequence for $S_1^{k=K}$ results after $\log_2(M)$ iterations. A pyramidal scale structure of merged new sets S_i^k (see Fig. 1) can now be obtained by using 1,2,4,. . . ,2^m subsequent subscans per reconstruction according to Eq. (1) and (3).

As an example, the sequence S_1^4 for $M = 16$ subscans together with its pyramidal scale structure with all possible S_i^k is given as follows:

$$\beta = \frac{\psi_\Delta}{16}\left(\underbrace{\underbrace{\underbrace{\underbrace{\underbrace{0}_{s_1^0},\underbrace{8}_{s_2^0}}_{s_1^1},\underbrace{\underbrace{4}_{s_3^0},\underbrace{12}_{s_4^0}}_{s_2^1}}_{s_1^2},\underbrace{\underbrace{\underbrace{2}_{s_5^0},\underbrace{10}_{s_6^0}}_{s_3^1},\underbrace{\underbrace{6}_{s_7^0},\underbrace{14}_{s_8^0}}_{s_4^1}}_{s_2^2}}_{s_1^3},\underbrace{\underbrace{\underbrace{\underbrace{1}_{s_9^0},\underbrace{9}_{s_{10}^0}}_{s_5^1},\underbrace{\underbrace{5}_{s_{11}^0},\underbrace{13}_{s_{12}^0}}_{s_6^1}}_{s_3^2},\underbrace{\underbrace{\underbrace{3}_{s_{13}^0},\underbrace{11}_{s_{14}^0}}_{s_7^1},\underbrace{\underbrace{7}_{s_{15}^0},\underbrace{15}_{s_{16}^0}}_{s_8^1}}_{s_4^2}}_{s_2^3}}_{s_1^4}\right). \tag{5}$$

Figure 2 graphically shows the distribution of the scanning angles for the sequence S_1^2 with $N = 16$ and $M = 4$.

2.2 *Golden-Ratio Decomposition*

The idea of organizing the projections using the Golden ratio was introduced by Köhler,[4] who used the scheme to organize the projections for iterative reconstruction methods. The method uses the Golden ratio $\phi = (1 + \sqrt{5})/2$ to determine the next acquisition angle. In this scheme, the acquisition angle of projection p_i is described by

$$\theta_i = i\,\phi\,\pi \bmod \pi. \tag{6}$$

The consequence of Eq. (6) is that two consequent projections in time are nearly orthogonally separated in rotation. By rotating the sample in this manner, every chronological contiguous subsequence of the projection data represents a

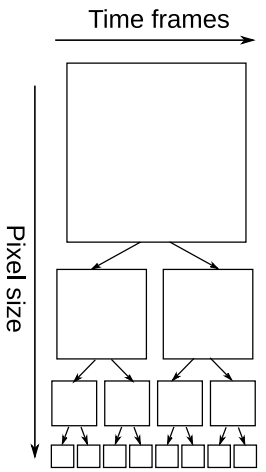

Fig. 1 Scale pyramid showing spatial versus temporal resolution allowed by nonsequential scan decomposition schemes.

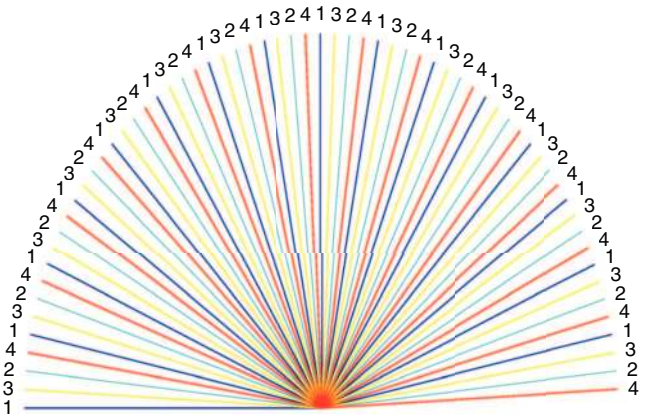

Fig. 2 Realization of the binary scan decomposition with $M = 4$ subscans and $N = 16$ projections in the single sparse subscan.

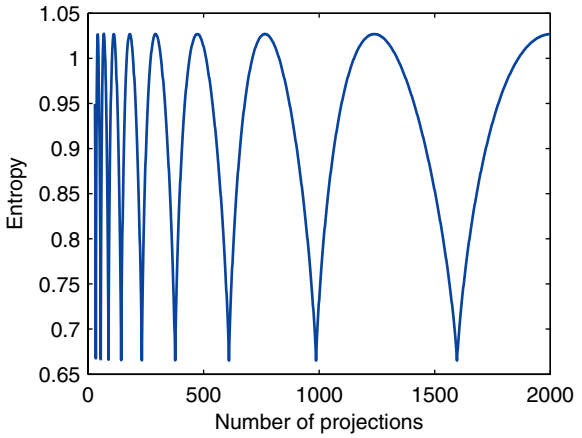

Fig. 3 Information theoretical entropy of the angular difference between two projections in a sorted subsequence.

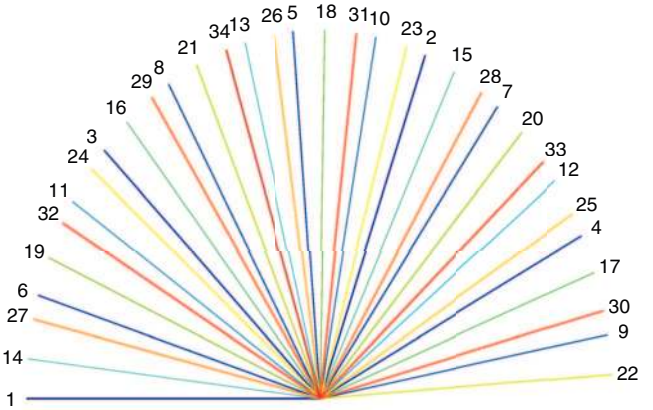

Fig. 4 Realization of the Golden ratio decomposition for $N = 34$.

complete coverage of the scan arc (π or 2π). This is an important feature for the ability to reconstruct the data with different spatiotemporal resolutions. This scheme can be started with no predefined end and arbitrarily terminated at any convenient end point.

2.2.1 *Irregular angle distribution*

To evaluate the distribution and coverage of the acquisition angles for different subsequence lengths, a numerical experiment was made. In the experiment, the information entropy [Eq. (7)] of the angle difference probability for a number of realizations was computed,

$$H(X) = -\sum_i p(x_i)\ \log[p(x_i)]. \tag{7}$$

The M subscan realizations Θ_i^N with length N and $i \in [0, M - 1]$ were computed using

$$\Theta_i^N = \{(i\,N + j) \cdot \phi \cdot \pi \bmod \pi \mid j \in [0, N - 1],\ j \in \mathbb{Z}^+\}. \tag{8}$$

Each set Θ_i was sorted, and the difference between adjacent angles was computed. For a $[0, 2\pi)$ scan, the modulo operation uses 2π instead of π. The histogram of these angle differences was then used in Eq. (7). An experiment with $M = 50$ resulted in the entropy curve shown in Fig. 3. This curve shows that the entropy varies between 0.66 and 1.027. These values corresponds to two distinct angle distance histograms. For the minima, two angle distances are present while for the maxima, three angle distances are present. The ideal case for filtered backprojection (FBP) is equidistant angles, which would result in $H(X) = 0$. The local minima in Fig. 3 indicates the ideal lengths of the subsequences for the spatiotemporal reconstructions. It can be noted that the locations of the local minima are found at subset sizes given by the Fibonacci numbers. This is related to filling complete levels of projections that are close to equidistant. In nature, the same pattern can be seen in the seed arrangement of a sunflower.[5] Figure 4 shows a realization for Θ_0^{34}, which corresponds to a local minimum in the entropy curve Fig. 3. In Fig. 4 it can be seen that the acquisition angles are almost uniformly distributed.

The effect of using a number of projections (N) given by a local minimum or a local maximum in the entropy curve is visualized in Fig. 5. The test consisted of reconstructing the sinogram of the eight-bit phantom [Fig. 5(a)] using different numbers of projections. Error images [Fig. 5(b) and 5(c)] are computed as the difference between the original phantom and the reconstructed images. The error images clearly show that the image corresponding to the local minimum has less reconstruction artifacts even though it uses 76% of the projections used for the image reconstructed at the entropy maximum.

2.3 *Weighting Scheme for Irregular Angles*

The FBP algorithm requires equidistant projections for best performance. The Golden ratio scan does not fulfill this requirement as shown in Sec. 2.2. To produce more accurate results, each projection must be weighted to correct for the deviation from the ideal position.

In postacquisition data processing, the first operation to determine the projection weights is to sort the sequence of acquisition angles. The sorted list (q) contains tuples $(q_j, i) = (\theta_i \bmod \pi, i)$. The first element (q_j) of the tuple is used as sorting key and, later, to compute the projection weight.

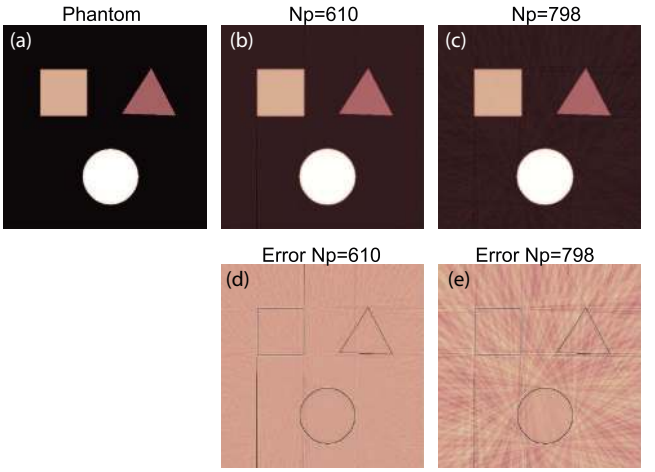

Fig. 5 Phantom image used for the test (a). Images reconstructed using (b) 610 and (c) 798 projections, respectively (gray-level interval $[-10, 260]$). The error images for the reconstructed images using (d) 610 and (e) 798 projections using the gray-level interval $[-10,10]$. The error is the difference between phantom and its reconstructed sinogram.

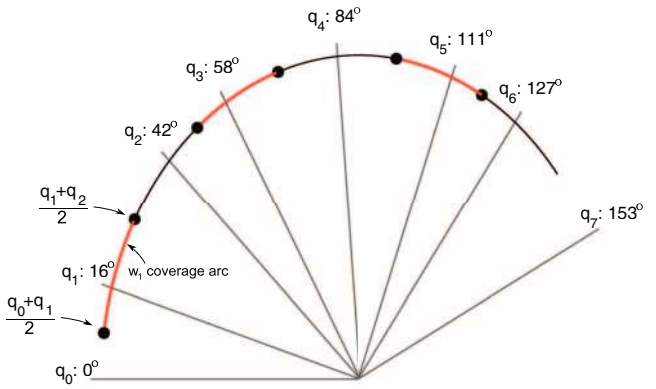

Fig. 6 Illustration of the projection weighting.

The index variable i is saved as the second element of the tuple and used to connect the weight to the correct projection. This information would otherwise be lost in the process of sorting the angles. The modulo operation is used to fold the projections in $[\pi, 2\pi)$ back into the interval $[0, \pi)$.

The weight w_j is computed using the sorted angle sequence q:

$$w_j = \frac{(q_{j+1} + q_j) - (q_j + q_{j-1})}{2(k\pi)} \quad j = [2, M-1]; \tag{9}$$

the index j indicates the position in the sorted list q. Figure 6 shows the coverage arcs for some weights. The value of k is 1 for a $[0, \pi)$ scan and 2 for a $[0, 2\pi)$ scan. The first and last elements in the list require some special handling,

$$w_1 = \frac{(k\pi - q_M) + (q_2 - q_1)}{2(k\pi)}, \tag{10}$$

$$w_M = \frac{(k\pi - q_M) + (q_M - q_{M-1})}{2(k\pi)}. \tag{11}$$

Using this weighting scheme, sparsely distributed projections will have greater impact on the result than denser distributed ones. We note that this weighting scheme is also appropriate for many other projection orderings, including random angle projection ordering. A further feature of this weighting scheme is that prematurely terminated scans can be reconstructed using all data.

Figure 7 shows the reconstruction of the same data as in Fig. 5, but here the weights from Eqs. (9)–(11) were applied to the sinogram. The images show that most of the streak artifacts that were found in the uncorrected images now are gone. The best improvement can be seen in the $N = 798$ image. Using the proposed weighting, the choice of N becomes less crucial for the image quality.

3 Experiment

3.1 *Sample Description and Data Acquisition*

In order to test the above-mentioned acquisition strategies with neutron tomography, three samples exhibiting a model dynamic process were prepared in a similar manner. Each sample consisted of an aluminum cylindrical sample container with an internal diameter of 10 mm, a height of 13 mm, and a wall thickness of 1 mm that served as a container for an assembly of lightweight aggregate (LWA) and superabsorbent polymer (SAP) particles.

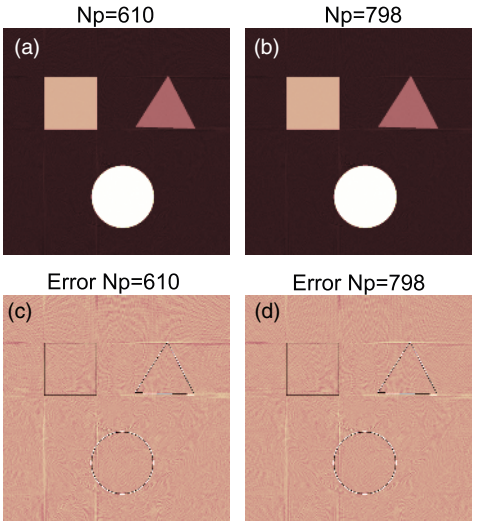

Fig. 7 Sinograms used in Fig.(5) reconstructed with the weighting scheme described in Eq. (9)–(11), (a) and (b). Error images for the reconstructed images are shown in (c) and (d) with gray-level interval $[-10,10]$.

Seven particles of D_2O-prewetted expanded clay LWA (Liapor) were first surfacedried using a soft tissue paper and then placed at the bottom of the aluminum container in a single layer. Three round SAP particles were allowed to absorb D_2O for several minutes, surface dried using a soft tissue paper, and placed as a second layer of the LWA. The sample was quickly transferred to the neutron tomography hutch for imaging; a fresh sample was used for each tomography experiment.

3.2 *Neutron Microtomography Test Arrangement*

The samples were scanned using the tomographic setup of the cold neutron-imaging beamline ICON, Kaestmer et al.[6] at the Paul Scherrer Institut, Switzerland, with a neutron beam neutron intensity of 1.3×10^7 neutrons $cm^{-2}\,s^{-1}\,mA^{-1}$, a mean energy of 8.53 meV, and a collimation ratio of L/D=343. The detector was composed of a 20-μm-thick gadolinium-oxysulfide (Gadox) scintillator screen and a CCD camera. The exposure time for each projection was 20 s, and the image pixel size was 13.5 μm.

In order to provide a reference measurement, the first sample was scanned using the traditional sequential acquisition strategy with 512 projections uniformly distributed over 180-deg rotation.

The second sample was scanned using the binary acquisition strategy (*cf.* Sec.2.1) with the same total number of projections $N \times M = 32 \times 16 = 512$. The size of the smallest subset S_i in the binary acquisition strategy was 16 projections ($M = 16$).

The third tomography experiment employed the Golden ratio acquisition strategy (*cf.* Sec.2.2). This experiment was terminated at 924 projections.

The replicate nature of the investigated sample assemblies, and the stable environmental conditions in the experimental hutch led in all three cases to a similar dynamic process. The water release from the originally water-saturated particle assemblies led to the decrease in the SAP diameter ~0.005 pixels/s. This rate translated to a motion of ~1 pixel in every

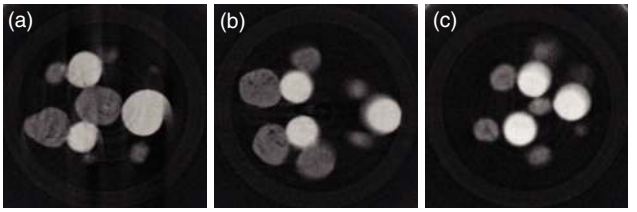

Fig. 8 Reconstructed slices of 512 projection data sets using (a) sequential, (b) binary decomposition, and (c) Golden ratio scan schemes.

10 projections, which was a large-enough displacement to cause significant motion artifacts in reconstructed images.

3.3 *Reconstruction*

As the spatiotemporal scanning schemes proposed above imply, high temporal resolution is associated with a low number of projections. In such cases, the Nyquist theorem Kak and Slaney,[3] and Nyquist[7] which states that the number of projections (N_p) should be related to the number of samples N_u for each projection with

$$N_\mathrm{p} = \frac{\pi}{2} N_u \tag{12}$$

cannot be fulfilled for the reconstructed image except for the regions close to the image center. This involves a considerable drop of the spatial resolution over the entire image. Different reconstruction algorithms respond differently to this situation. In particular, FBP, Kak and Slaney,[3] which is most popular due to its time efficiency, produces strong streak artifacts.

The flat and dark-field corrected projections were therefore reconstructed using an algebraic reconstruction technique (ART) based on the penalized likelihood image reconstruction.[8] A reconstruction obtained by FBP was used as the initial approximation in this iterative algorithm. In this approach, the failure to fulfill the Nyquist theorem causes blurring of the structural details rather than introducing additional erroneous pattern. FBP was therefore mainly used in the case of large numbers of projections.

4 Results

4.1 *Motion Artifacts*

The reconstruction of the full projection sets, comprising 512 projections, are presented in Fig. 8, showing one single slice through the image volumes received with the sequential [Fig. 8(a)], binary decomposition [Fig. 8(b)], and Golden ratio [Fig. 8(c)] acquisition schemes. Sequential strategy leads to clear snail-shell like artifacts that are typical for the motions of a shrinking sphere [see Fig. 8(a)]. These artifacts affect the image quality even in the regions outside the locations where motions occurred. As is evident for both proposed alternative schemes, binary decomposition and Golden ratio, the motion artifacts now manifest themselves as blurring contained only within the altering regions. The shrinking volume is presented as a gray-level

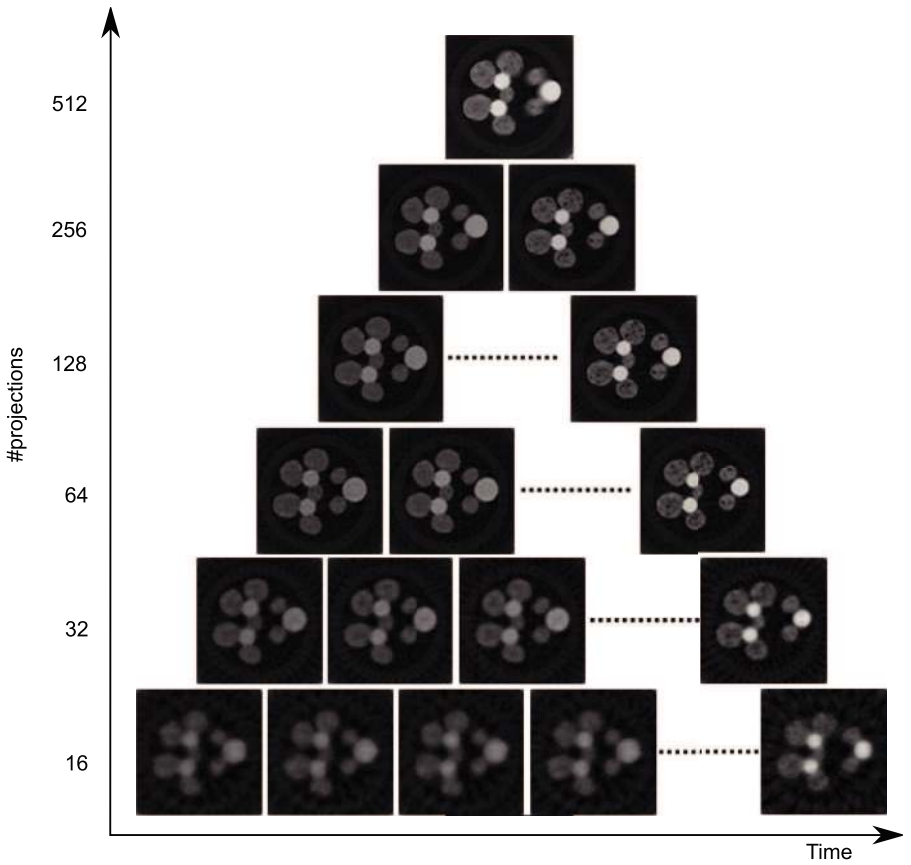

Fig. 9 Scale pyramid of a volume recorded by a binary decomposition scheme. The possible balances between spatial and temporal resolution are demonstrated in these reconstructions of a single tomography data set. The bottom row shows a few of the 16 time steps available with the low spatial resolution option. In this pyramid, image size is fixed and printed resolution is allowed to vary.

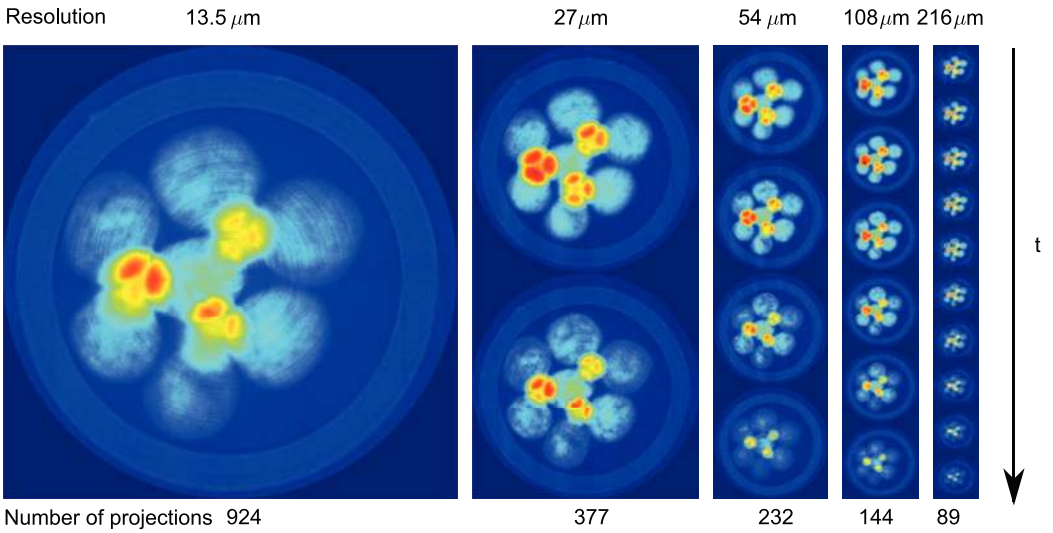

Fig. 10 A fresh sample imaged with the Golden ratio scheme. Because most of the sample motion is expected within particle layers and to increase the image signal-to-noise ratio, the reconstruction images are shown here as the cumulated sum along the sample rotation axis; the sum image generates the additional detail, such as the contacts between SAP and LWA particles. The pixel size and number of projections used to reconstruct each image are appended at the top and bottom rows. In this pyramid, printed resolution is fixed and image size is allowed to vary, in contrast to Fig. (9).

gradient within the sample (i.e., the artifacts are confined within the largest sample boundaries). In particular, note the bright SAP particles, which are noticeably decreasing in size. Hence, ongoing processes during monitoring do not degrade the images when using the proposed acquisition schemes.

4.2 *Exploiting the Spatiotemporal Potential*

As discussed in Sec. 2, the binary decomposition and Golden ratio schemes allow for retrieval of spatiotemporal information from a single tomography scan. Moreover, the balance between spatial and temporal resolutions can be selected during data processing, leaving data acquisition relatively unconstrained by the as-yet unknown dynamics of the sample to be imaged.

Data from a single tomography experiment, acquired with the binary decomposition scheme, can be processed as described in the Fig. 1 scale pyramid so as to show the many possible options of spatial versus temporal resolution.

Figure 9 shows the scale pyramid of spatial versus temporal resolution as designed in Fig. 1. The topmost figure gives the greatest spatial resolution for the static components in the image, whereas the bottom row gives the best temporal resolution for the dynamic components in the sample. In fact, a user may wish to select several options, one to highlight object positions and another to calculate rate of change of the objects.

Figure 10 shows the strength of pyramidal reconstruction by displaying results from a Golden ratio scan. The number of projections in each subset was selected to give the least angular entropy according to Fig. 3. The many possible reconstructed 3-D data sets are represented as cumulative 2-D projections along the z-axis (i.e., the acquisition axis of the volume). The FBP method was used for these reconstructions with the projection weights given in Eqs. (9)–(11). The leftmost image shows the volume at highest spatial resolution while the subsequent rows show the time series of the ongoing process during data capture, yet at lower spatial resolutions.

Figure 11, shows two of the eight 3-D renderings of subsets from the pyramidal volumetric data, as it was attained from the binary decomposition scheme. The data volumes are reconstructed from sets of 64 projections by ART, each yielding eight time frames.

For tomography data acquired with both the binary decomposition and the Golden ratio schemes, three types of ongoing processes occurring during acquisition time are observed. These are (i) the shrinkage of the SAP particles (three bright spheres in the top layer), (ii) the formation of spherical patterns within the LWA particles due to water desorption (seven dark particles in the bottom layer), and (iii) the coupled translation motions of all particles.

Figure 12 shows single slices through each of the eight 3-D volumes, including the initial and final conditions as represented in Fig. 11. They are all taken at the same height (i.e., level on the z-axis). Both particles types, SAP (bright) and LWA (dark) particles are transected. As in Fig. 11, the dynamic process of water release from the originally saturated particles and their corresponding spatial motions are clearly visible. In contrast to Fig. 8, the motion artifacts are suppressed to low levels. There are two reasons for the suppression: (i) the proposed alternative schemes are much more tolerant to motions during data acquisition (see Sec. 4.1), and (ii) the selected volume sampling rate is

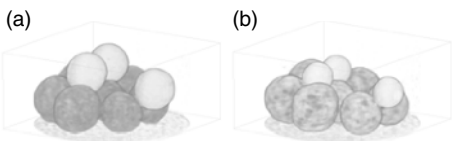

Fig. 11 3-D representations of the (a) initial and (b) final conditions created from the binary decomposition scheme using 64 projections per 3-D frame.

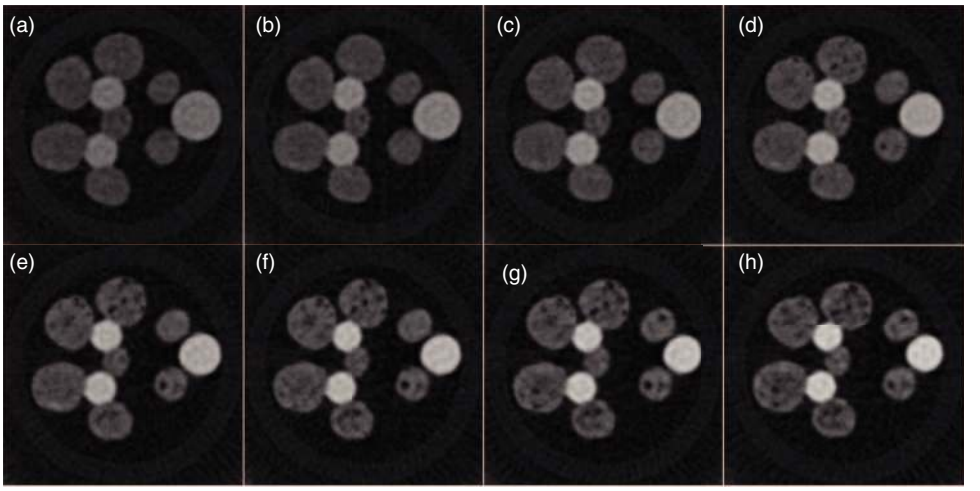

Fig. 12 Slices through 3-D data volumes created from the binary decomposition scheme with 64 projections per slice.

sufficient to capture the dynamic process. At the same time, the image sequence demonstrates that sufficient spatial resolution can still be attained at low numbers of projections in the case when using a low-noise amplification reconstruction technique.

4.3 *Application of the Golden Ratio to Polymer Blend Imaging with Synchrotron X-ray Tomography*

There has been an interest in polymer blends made from polystyrene and thermodynamically compatible flame retardants.[9] Some blends were prepared with intentionally poor initial mixing and tomography was used to study the dissolution of the flame retardant in the blend.[10] Cylindrical samples are observed with synchrotron x-ray tomography with *in situ* heating. In addition to dissolution, the sample is observed to swell and slump during the tomography data acquisition. It is extremely convenient to begin the tomography acquisition with the Golden ratio scheme and terminate the run at the end of the available beam time. Then, time windows are assigned based on estimated sample motion and image signal-to-noise ratios. Figure 13 shows a slice from the sixth time window and the reconstructed volume after ten time windows. Figure 13(a) shows the deleterious effect of minor sample motion during a time window, yet the results are still sufficiently accurate to enable tracking of 20 undissolved flame retardant particles [Fig. 13(b)]. The original location of the polymer cylinder is outlined by the semi-transparent surface.

5 Discussion

The experiments show that both decomposition schemes, binary and Golden ratio, are less sensitive to motion during data acquisition. In both approaches, the affected regions are blurred only within the boundaries where motions occur.

With regard to the reconstructibility of the projection sets, the binary scheme is privileged with regard to the equispaced angular sequence. In the case of Golden ratio scans, deviations from equidistant angles will require projection weighting as described by Eqs. (9)–(11).

The utilization of the binary and the Golden ratio acquisition strategies might be limited by the fact that their respective total sample rotations are significantly larger than the one of the standard sequential acquisition strategy. In the case of the experiments reported in this paper, the total sample rotation was equal to about π, 59π, and 241.5π, for the sequential, the binary, and the Golden ratio strategies, respectively. For suitable use of binary and Golden ratio strategies, the exposure and readout times must be such that the total

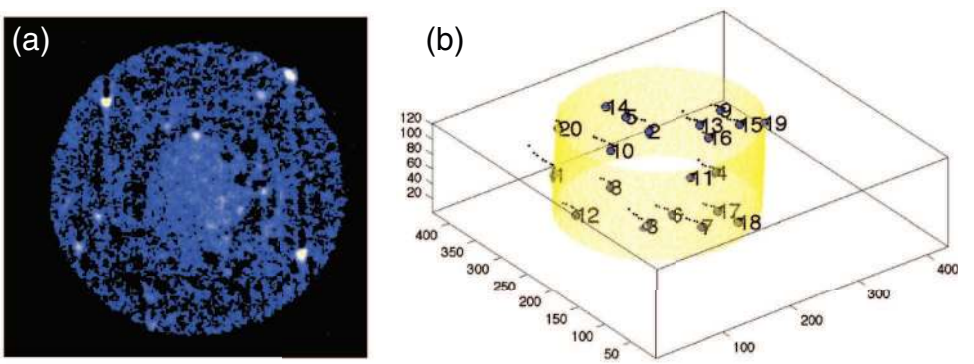

Fig. 13 Dissolution of a flame retardant into polystyrene is monitored with synchrotron x-ray tomography while heated. Even though the sample is moving during acquisition, high-quality images can be (a) obtained and (b) compiled over time for particle tracking. The semi-transparent surface indicates the initial surface of the sample.

acquisition time is not significantly increased by the time necessary for sample rotational positioning. This is usually true for the neutron tomography experiments in which (*i*) the exposure time is significantly longer than the time necessary for the sample rotation and (*ii*) the majority of the sample rotation occurs during the detector readout time. However, such conditions may not be met in the case of other types of computed tomographies (such as synchrotron-based x-ray tomography).

Yet, with respect to the flexibility, the Golden ratio decomposition scheme outperforms the binary scheme, because the number of scans per reconstruction can basically be selected arbitrarily, even though certain optimum numbers regarding to equidistance turn out to be preferable.(Sec. 2.2.1) Thereby, for the reconstruction, the optimal spatial resolution can be chosen at an arbitrary time frame. Furthermore, the duration of a Golden ratio scan can be varied. This means that for experiments with unknown length, the acquisition can continue until the process has ended or until a certain time slot of registered beamtime expires.

The great flexibility of the presented schemes, in particular, the Golden ratio decomposition, enables the reconstruction of entire pyramids of varying spatiotemporal resolution instead of just one single image, as in the case of the ordinary sequential projection data. However, this flexibility may lead to the reconstruction of an enormous amount of image data. This may also involve huge reconstruction times, because time-consuming iterative reconstruction algorithms are preferable to FBP, especially for a reduced number of projections. The future work may focus on efficient determination of the optimal path in the spatiotemporal reconstruction pyramid.

6 Conclusions

The paper presents two alternative acquisition strategies that are suitable for the assessment of spatiotemporal 3-D image information. The first one is based on binary interleaved acquisition schemes, and the second one is based on a Golden ratio angular sequence. They hold the potential for the acquisition of dynamic processes by means of CT, as it was verified on projection sets from particle arrangements acquired by means of cold neutron CT. The sequences permit both, alleviation of motion artifacts, as well as a posteriori monitoring of dynamic processes in three dimensions, while allowing the selection of appropriate spatial or temporal resolution. They are thus suitable for recording motions and for surveying structural changes in processes of originally unknown or variable dynamics.[11]

Acknowledgments

The authors kindly thank Professor Adel Faridani, Oregon State University, for fruitful discussions. The authors also kindly acknowledge BASF Construction Chemicals GmbH, Trostberg, Germany, for production of tailor-made SAP particles for the experiment. We (LGB) thank the support of the U.S. National Science Foundation (Grant No. CHE-0910937) for support of materials science tomography.

References

1. S. S. Vedam, P. J. Keall, V. R. Kini, H Mostafavi, H. P. Shukla, and R. Mohan, "Acquiring a four-dimensional computed tomography dataset using an external respiratory signal," *Phys. Med. Biol.* **48**, 45–62 (2003).
2. E. Reitzel, T. Pan, and G. T. Y. Chen, "Four-dimensional computed tomography: image formation and clinical protocol," *Med. Phys.* **32**, 874–889 (2005).
3. A. C. Kak and M. Slaney, *Principles of Computerized Tomographic imaging*, IEEE, Piscataway, NJ (1988).
4. T Köhler, "A projection access scheme for iterative reconstruction based on the golden section," *IEEE Nuclear Science Symp. Conf. Record*, Vol. 6, 3961–3965 (2004).
5. M. Livio, *The Golden Ratio – The Story of the World's Most Astonishing Number*, Broadway, (2002).
6. A. P. Kaestner, S. Hartmann, G. Kühne, G. Frei, C. Grünzweig, L. Josic, F. Schmid, and E. H. Lehmann, "The ICON beamline – a facility for cold neutron imaging at SINQ," *Nuclear Instruments and Methods in Physics Research Section A* **659**(1), 387–393 (2011).
7. H. Nyquist, "Certain topics in telegraph transmission theory," *Trans. Am. Inst. Elect. Eng.* **47**, 617–644 (1928).
8. S. Ahn, J. A. Fessler, D. Blatt, and A. O. Hero, "Convergent incremental optimization transfer algorithms: Application to tomography," *IEEE Trans. Med. Imaging* **25**, 283–296 (2006).
9. K. Ham, H. Jin, R. Al-Raoush, X. Xie, C. S. Byerly, G. R. Willsonand, L. S. Simeral, M. L. Rivers, R. L. Kurtz, and L. G. Butler, "Three-dimensional chemical analysis: Synchrotron tomography at multiple X-ray energies of brominated aromatic and antimony oxide additives in polystyrene," *Chem. Mater.* **16**, 4032–4042 (2004).
10. H. A. Barnett, K. Ham, J. T. Scorsone, and L. G. Butler, "Synchrotron x-ray tomography for 3D chemical distribution measurement of a flame retardant and synergist in a fiberglass-reinforced polymer blend," *J. Phys. Chem.* **114**, 2–9 (2010).
11. P. Trtik, B. Münch, W. J. Weiss, A. Kaestner, I. Jerjen, L. Josic, E. Lehmann, and P. Lura, "Release of internal curing water from lightweight aggregates in cement paste investigated by neutron and X-ray tomography," *Nucl. Instrum. Methods Phys. Res. Sect. A* **651**(1), 244–249 (2011).

Anders Kaestner is a beamline scientist at the cold neutron imaging beamline (ICON) at Paul Scherrer Institut, Switzerland. He started in imaging and image processing with a PhD in signal processing at Chalmers Institute of Technology, Gothenburg, Sweden, in 2002. This topic was continued as a postdoctoral student working with image-processing tasks for soil science at the Swiss Federal Institute of Technology in Zürich, Switzerland. Special fields of interest to him are computed tomography and image enhancement.

Beat Münch is a scientist at the Laboratory for Concrete and Construction Chemistry, Empa, Switzerland, in the area of applied image modeling. He was awarded a PhD in medical imaging and since has been involved in miscellaneous interdisciplinary research areas, such as color science, newsprint, porosity and particle analysis, and tomography. His special expertise encompasses computer-based quantitative evaluation and structural analysis of 3-D image volumes from gray-level and color images.

Pavel Trtik is a scientist at the Laboratory for Concrete and Construction Chemistry, Empa, Switzerland. He studied civil engineering, completed PhD at Advanced Concrete and Masonry Centre, University of Paisley, Scotland, and was a postdoctoral student at ETH Zurich, Switzerland. He has recently been named associate professor at his alma mater, Czech Technical University in Prague. His research interests include the use of 3-D imaging techniques for investigation of the structure-property relationships of building materials.

Les Butler is a professor of chemistry at Louisiana State University (LSU) in Baton Rouge, Louisiana, researching applications of tomography to materials science problems. He started in solid-state NMR spectroscopy with a PhD at the University of Illinois at Urbana-Champaign in 1981, was a postdoctoral student at CalTech, and then a faculty member at LSU. He was drawn to imaging by friends in NMR imaging and then built a tomography beamline at the LSU synchrotron in 2000.